JACS
JOURNAL OF THE AMERICAN CHEMICAL SOCIETY

ARTICLE

pubs.acs.org/JACS

Morphology Design of Porous Coordination Polymer Crystals by Coordination Modulation

Ayako Umemura,[†] Stéphane Diring,[†,‡] Shuhei Furukawa,[*,†,‡] Hiromitsu Uehara,[†] Takaaki Tsuruoka,[†,§] and Susumu Kitagawa[*,†,‡]

[†]ERATO Kitagawa Integrated Pores Project, Japan Science and Technology Agency (JST), Kyoto Research Park Bldg #3, Shimogyo-ku, Kyoto 600-8815, Japan

[‡]Institute for Integrated Cell-Material Sciences (iCeMS), Kyoto University, Yoshida, Sakyo-ku, Kyoto 606-8501, Japan

[§]Frontiers of Innovative Research in Science and Technology (FIRST), Konan University, 7-1-20, Minatojima-minamimachi, Chuo-ku, Kobe 650-0047, Japan

Supporting Information

ABSTRACT:

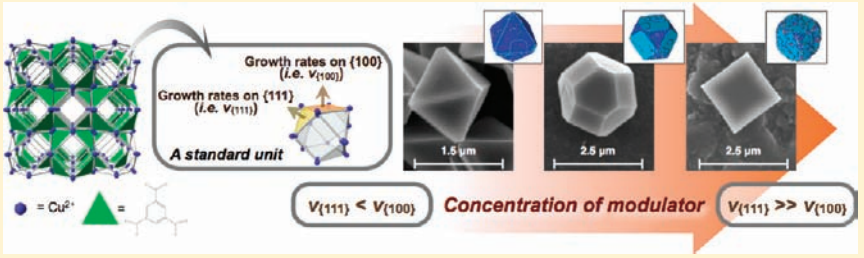

The design of crystal morphology, or exposed crystal facets, has enabled the development (e.g., catalytic activities, material attributes, and oriented film formation) of porous coordination polymers (PCPs) without changing material compositions. However, because crystal growth mechanisms are not fully understood, control of crystal morphology still remains challenging. Herein, we report the morphology design of $[Cu_3(btc)_2]_n$ (btc = benzene-1,3,5-tricarboxylate) by the coordination modulation method (modulator = *n*-dodecanoic acid or lauric acid). A morphological transition (octahedron−cuboctahedron−cube) in the $[Cu_3(btc)_2]_n$ crystal was observed with an increase in concentration of the modulator. By suitably defining a coarse-grained standard unit of $[Cu_3(btc)_2]_n$ as its cuboctahedron main pore and determining its attachment energy on crystal surfaces, Monte Carlo coarse-grain modeling revealed the population and orientation of carboxylates and elucidated an important role of the modulator in determining the ⟨100⟩- and ⟨111⟩-growth throughout the crystal growth process. This comprehension, in fact, successfully led to designed crystal morphologies with oriented growth on bare substrates. Because selective crystal orientations on the bare substrates were governed by crystal morphology, this contribution also casts a new light on the unexplored issue of the significance of morphology design of PCPs.

INTRODUCTION

On account of the relevance and beauty of biomineralizations and snow crystals,[1] particular emphasis has recently been placed on the control of crystal morphology, because in many cases it allows the properties to be tuned without changing the material composition. For instance, the improvement of capabilities of gold or silver nanoparticles for surface plasmon resonance,[2] semiconductor nanodots for the quantum confinement effect,[3] and metal or metal oxides for catalytic activity[4] is strongly dependent on crystal morphology. In the case of porous materials such as zeolites, the crystal morphology or the facet exposed to the external surface is of significance for their catalytic activity, because the reaction not only requires diffusion but also the availability of active sites that are embedded into the framework scaffold.[5]

Porous coordination polymers (PCPs) or metal−organic frameworks (MOFs), assembled by organic ligands with metal ions,[6] are an intriguing class of porous materials for gas sorption,[7] separation,[8] catalysis,[9] and sensors[10] because their framework topologies and pore sizes can be designed by an appropriate selection of metal geometry and structures of organic ligands. To date, a number of efforts have been made to control the crystal size for the improvement of the porous property and the expansion of their unconventional usability in biological applications[11] and electronics.[12] However, due to the lack of knowledge about their crystal growth mechanisms, the control of crystal morphology still remains challenging.[13] Although a few studies highlighted the importance of the crystal aspect ratio on the sorption properties,[14] there is no example where the control of exposed crystal facets was achieved despite its potential for the

Received: May 8, 2011
Published: August 23, 2011

Scheme 1. Coarse-Grain Modeling To Study Crystal Growth Habits As Investigated by the Relative Growth Rates of Surface Terraces as Modulator Influences[a]

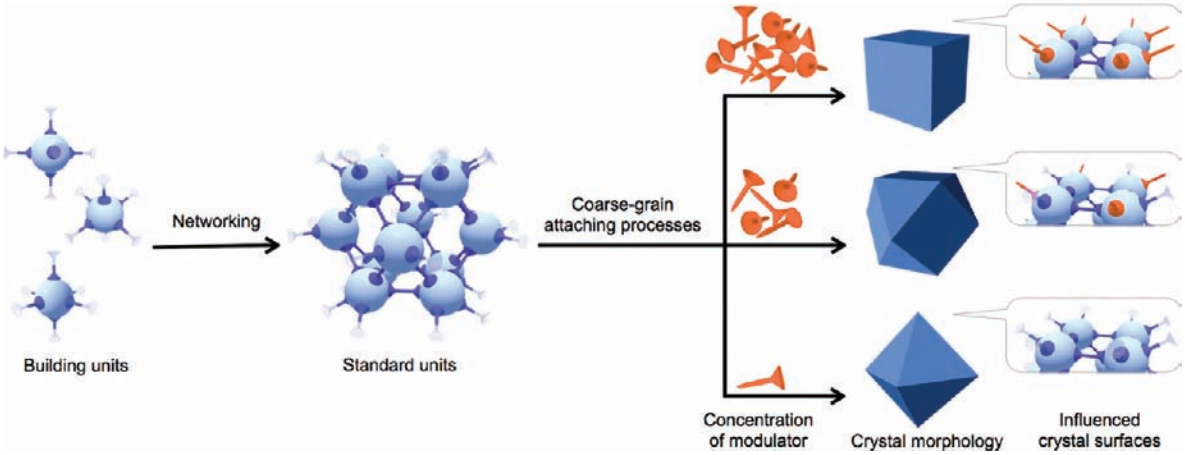

[a] An important step is in defining a standard unit whose arrangement is determined by building units such as SBUs that are networked in a framework structure.

improvement of catalytic activities,[9d,15] mechanical attributes,[16] and oriented film formation.[17]

Currently, the most reasonable prediction of crystal morphology has been performed by relative growth rates of the crystal face orientations.[18] These growth rates of orientations are proportional to the attachment energy of growth units. Unlike metal nanocrystals that are described as a sphere packing model where atoms are simply approximated to the isotropic sphere and recognized as growth units, PCPs inherently have rather complicated topologies. Whereas the secondary building unit (SBU) concept has been well accepted to anticipate and clarify the PCP topology,[19] SBUs cannot simply be regarded as growth units, as they are intricately oriented in the network. In order to determine crystal morphology of PCPs, a further simplified coarse-grained standard unit can suitably be defined from the topological analysis of framework structure. As the standard unit associates with neighboring units in the network, the attachment energy on crystal surfaces can be relatively classified by their connectivities. By applying the attachment energy of standard units in the stochastic process of the Monte Carlo (MC) method, coarse-grain modeling ultimately leads to the understanding of the effect of the assembly of standard units on the resulting crystal morphology and thus the understanding of the underlying crystal growth mechanism.

We recently induced rod-like crystal morphology in the tetragonal crystal system, $[Cu_2(ndc)_2(dabco)]_n$,[20] where two different coordination bonds participated in the framework formation (ndc =1,4-naphthalenedicarboxylate; dabco =1,4-diazabicyclo-[2.2.2]octane).[21] By the use of monocarboxylic acid as an additive (modulator), only the coordination between Cu-ndc was perturbed by the modulator, leading to the anisotropic crystal growth. In this case, we could simply consider a cuboid as a standard unit, and the resulting rod-like morphology was explained by interference with its connectivity along the ⟨100⟩ directions. Here we target a more complicated framework system with twisted boracite topology (tbo),[22] $[Cu_3(btc)_2]_n$ (btc = benzene-1,3,5-tricarboxylate),[23] and demonstrate the morphological transition with various expositions of crystal facets, octahedron−cuboctahedron−cube, by the coordination modulation method.[21,24] We elucidate the transition mechanism by the implementation of coarse-grain model based on a cuboctahedron standard unit defined from the topological analysis of $[Cu_3(btc)_2]_n$ framework structure and discuss the role of the modulator throughout the crystal growth process (Scheme 1). Furthermore, we demonstrate a first example of selective crystal orientation on a bare substrate by controlling only crystal morphology. We expect that this straightforward approach by morphology design will allow significant potentials for the application of PCPs in crystal engineering as well as for the properties by controlling exposed crystal facets such as catalytic activity.

EXPERIMENTAL SECTION

Materials. Reagents and solvents were purchased from commercial sources and used without further purification.

Preparation of $[Cu_3(btc)_2]_n$ Crystals. Copper(II) nitrate trihydrate ($Cu(NO_3)_2 \cdot 3H_2O$; 41.0 mg, 0.17 mmol) and lauric acid [0; 2.34 mmol (475.5 mg); 4.75 mmol (951 mg); 7.13 mmol (1.4275 g); 9.5 mmol (1.902 g) and 11.88 mmol (2.3775 g), namely LA-0, 25, 50, 75, 100, and 125, respectively] were dissolved in 10 mL of butanol in 20 mL Pyrex microwave vials. The mixed solution was heated with a heat-gun until a transparent solution was obtained. Benzene-1,3,5-tricarboxylic acid (20 mg, 0.095 mmol) was added, and the mixture was heated by microwave irradiation (Initiator 2.5 microwave from Biotage) at 413 K for 60 min. The resulting blue powder was isolated by centrifugation and washed with ethanol (3 × 10 mL).

Powder X-ray Diffraction Measurement. The light-blue solids obtained were dried for 3 h at 20 mbar at room temperature before analysis. The diffraction data were collected on a Bruker Model D8 Discover apparatus with GADDS equipped with a sealed tube X-ray generator producing Cu Kα radiation (λ = 1.54 Å).

X-ray Diffraction Measurement for Oriented Crystals on Substrates. The diffractions were collected using SmartLab (Rigaku) equipped with a rotating anode Cu Kα X-ray generator. The measurements were performed in the $\theta/2\theta$ out-of-plane mode (2θ = 5−20°) with a step-size of 0.02° for 2θ and a scan-rate of 0.02° s^{-1} for 2θ, and in the in-plane mode with a step-size of 0.024° for 2θ and a scan-rate of 0.004° s^{-1} for 2θ.

Field-Emission Scanning Electron Microscopy. The light-blue solids stored in ethanol were dispersed and deposited on a carbon

slab (99.99% purity) and then coated with osmium prior to measurement. The images were obtained from a JEOL Model JSM-7001FA or JSM-75FCT SEM system operating at 5.0 to 15.0 kV.

Gibbs Free Energy for Monte Carlo Simulation. The morphological importance is determined by the fundamental habit of crystal growth. BFDH (Bravais, Friedel, Donnay, and Harker) law states, with the orientation (*hkl*) of crystal, that the growth velocity of a facet is inversely proportional to the lattice spacing, d_{hkl}. In other words, the slowest growing faces dominate the growth morphology of the crystal. Therefore, crystal morphology can be relatively decided by the 2D-nucleus on each crystal facet, shown by probabilities for growth, P_i^G, and dissolution, P_i^D, at a specific site type, *i*. Crystals should constantly grow in a certain direction with determined relative energies unless some energetic conditions are changed, such as supersaturation and temperature, in a closed system. However, supersaturation or driving force of crystallization shows dynamics during crystal growth, which can be discussed in thermodynamics. In order to adapt this energetic condition,

$$\frac{P_i^G}{P_i^D} = \exp\left(-\frac{\Delta E_i}{k_B T} - \frac{\Delta \mu}{k_B T}\right) \quad (1)$$

is used for the Gibbs free energy for MC simulation. In this way, the relative energy, ΔE_i, between the specific site type, *i*, and a standard energy level can independently be calculated from the driving force, $\Delta\mu$, where k_B and T are the Boltzmann constant and temperature in Kelvin, respectively. Dividing equally into a growth event and a dissolution event at equilibrium, the variation of entropy (i.e., relative supersaturation) was efficiently evaluated, taking one half of each energetic term.[18b,24]

$$P_i^G = exp(0.5\frac{\Delta E_i}{k_B T} + 0.5\frac{\Delta \mu}{k_B T}) \quad (2)$$

$$P_i^D = exp(-0.5\frac{\Delta E_i}{k_B T} - 0.5\frac{\Delta \mu}{k_B T}) \quad (3)$$

In this manner, during the crystal growth process, the driving force is shifting from high to low supersaturations at a constant growth rate in the calculation. A balanced position is then found between growth and dissolution events owing to the Ostwald ripening, which is the so-called equilibrium. All data shown in this report were calculated based on $(\Delta E_{i-1} - \Delta E_i) = 5$ kcal/mol ($1 \le i \le 12$; $i = 0$ as an initial nucleation site) performed for 1 million MC times for each case.

Computing. The connectivity network of the $[Cu_3(btc)_2]_n$ coarse-grain model was formulated in Fortran 90, and the Gibbs free energy was applied for the calculation run on Fujitsu HX600 cluster at Kyoto University (61.2 TFlops of FP performance at peak; 32 GB RAM memory and 60 GB disk space allocated per contract). The data obtained were visualized with MacMegaPov v1.2.1 r3.

UV−vis Spectroscopy. The UV−vis solutions were prepared by dissolving various amounts of lauric acid (LA-0, 25, 50, 75, 100, and 125) in a copper nitrate solution in butanol (1.7×10^{-2} M). The UV−vis absorption spectra were obtained with a JASCO V-670 spectrophotometer.

Immobilization of $[Cu_3(btc)_2]_n$ on Gold-Coated Quartz Substrates. Commercial gold-coated quartz substrates were used. A solution of copper(II) nitrate trihydrate in butanol (41.0 mg, 5 mL, 0.17 mmol) mixed with lauric acid (LA-50, 4.75 mmol or LA-125, 11.88 mmol) was added to a suspension of benzene-1,3,5-tricarboxylic acid in butanol (20 mg, 5 mL, 0.095 mmol). The gold-coated substrate was placed in 1 mL of the mixed solution and 0.5 mL of ethanol and then incubated at 318 K for two days. The resulting crystals grown on the gold-coated substrate were washed with ethanol.

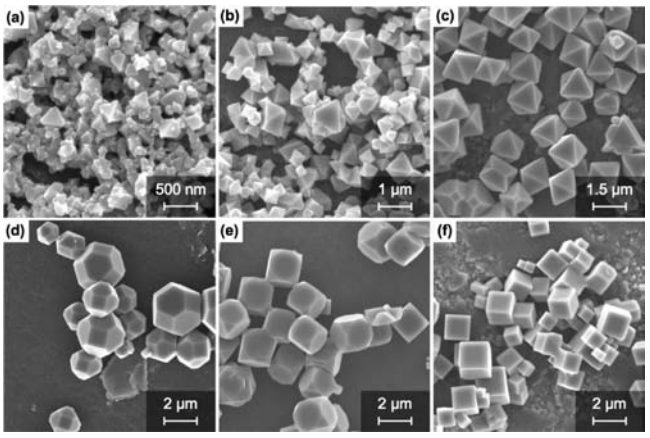

Figure 1. FESEM images of $[Cu_3(btc)_2]_n$ synthesized from copper nitrate under the condition of LA-*x*; *x* = (a) 0, (b) 25, (c) 50, (d) 75, (e) 100, and (f) 125.

RESULTS AND DISCUSSION

We previously succeeded in the kinetic control of crystal growth of $[Cu_3(btc)_2]_n$ by the coordination modulation method (modulator = *n*-dodecanoic acid or lauric acid) to tune the crystal size, using copper acetate as a metal precursor.[26] Copper acetate produces $[Cu_3(btc)_2]_n$ with fast nucleation and slower growth presumably because copper acetate already bears the preorganized paddlewheel structure,[27] resulting in ill-defined crystal morphology in the absence of kinetic control. In this study, we selected copper nitrate as a metal source to control the crystal morphology of $[Cu_3(btc)_2]_n$ with various concentrations of monocarboxylic acid as modulator (denoted as LA-*x*; *x* = [lauric acid]/[btc] molar ratio). Because the reaction of copper nitrate with btc ligand gives slow nucleation and then faster crystal growth,[28] the resulting $[Cu_3(btc)_2]_n$ is inherently obtained with better-defined morphology compared to copper acetate as a metal source. In order to focus on the role of modulator, other conditions (global concentration, temperature, solvent, and reaction time) remained unchanged.

A Trend of Crystal Morphology Caused by the Concentration of Modulator. Because the early stage of crystallization influences the crystal growth habit, the process starting from nucleation to the production of primary nanocrystals was examined in this study. The crystallization is understood by both kinetics in crystal nucleation and by the thermodynamically stable phase at equilibrium. In order to take the role of modulator into account, we first clarified the tendency of $[Cu_3(btc)_2]_n$ crystal morphologies through the coordination modulation method.

Figure 1a to 1f shows the field emission scanning electron microscopic (FESEM) images of $[Cu_3(btc)_2]_n$ synthesized from copper nitrate under various conditions of modulator, LA-0, 25, 50, 75, 100, and 125, respectively. The powder X-ray diffraction data of these crystals is summarized in Figure S1, Supporting Information. The competitive interaction brought by the monocarboxylic additive leads to the alteration of the nucleation process, the rate of which could be tuned by varying the concentration of modulator. As seen in Figure 1 in the region between LA-0 and 50, crystal size increased with the concentration of modulator, while the octahedral morphology remained unchanged. On the other hand, the $[Cu_3(btc)_2]_n$ crystals showed a morphology transition with a further increase in the concentration of modulator. From LA-50 to 125, the crystal size remained almost

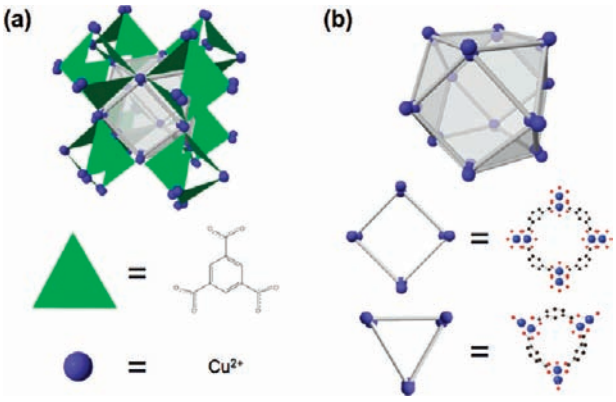

Figure 2. (a) The open-framework structure of $[Cu_3(btc)_2]_n$ in a unit cell composed of side pockets (constructed by btc-ligands and copper-metal sources) and a main pore (surrounded by those side pockets). (b) The main pore of $[Cu_3(btc)_2]_n$ (i.e., cuboctahedron) is composed of square-windows and triangle-windows. Red, blue, and black spheres represent oxygen, copper, and carbon, respectively. Hydrogen is omitted for clarification.

unchanged; however, an evolution of crystal morphology was observed: octahedron (LA-50), cuboctahedron (LA-75), truncated cube (LA-100), and cube (LA-125). This can be explained by the thermodynamic stability of growth facets.

Crystal shapes can be determined under the fundamentals of BFDH (Bravais, Friedel, Donnay, and Harker[29]) law. A crystal shape is arranged by the coexistence of slower and faster growth facets. As the crystal grows, the crystal gradually shapes the structure surrounded by the facets of slower growth. A cube is composed of six square facets of {100}, whereas an octahedron is surrounded by eight triangle facets of {111}. A cuboctahedron is seen as an intermediate stage between a cube and an octahedron. When the growth rate on {100} is faster than that on {111} (denoted as $v_{\{111\}} < v_{\{100\}}$), the crystal morphology will be surrounded by {111} faces and therefore presents an octahedron. Similarly, when $v_{\{111\}} > v_{\{100\}}$, a cube will be produced. If $v_{\{111\}} \approx v_{\{100\}}$, {111} and {100} faces equally grow, eventually showing a cuboctahedron. Throughout the course of crystallization for the LA-125 sample, the crystal morphology was constantly observed as a cube as shown in Figure S2, Supporting Information. Considering the BFDH law, the growth rate on each facet is assumed to be constant throughout the growth.

Implementation of $[Cu_3(btc)_2]_n$ Coarse-Grain Model To Elucidate the Effect of the Modulator on Crystal Morphology. In order to elucidate the correlation between the modulator concentration and the thermodynamic stability of facets, we carried out a coarse-grain modeling. A symmetrical crystal framework structure is constructed of a simplified building unit with its neighboring network (i.e., connectivity). When the growth direction of the building unit (i.e., growth unit) is involved, a crystal morphology is presented. Verified by the course of crystallization in $[Cu_3(btc)_2]_n$, crystal morphology was observed as constant throughout the growth. Therefore, crystallization processes can be simulated from the attachment energies of the growth unit by a stochastic process of the MC method, leading to the essential thermodynamic discussion.

Our target framework, $[Cu_3(btc)_2]_n$ possesses dinuclear copper paddlewheel units as SBUs, which are arranged in a face-centered cubic (fcc) network ($Fm\bar{3}m$). Figure 2a shows a schematic representation of a unit cell, $[Cu_3(btc)_2]_n$, consisting of tetrahedral

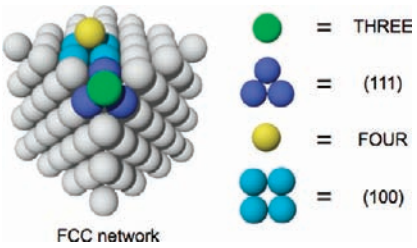

Figure 3. Face-centered cubic (fcc) network expressed by spheres. Significant spheres are shown in colors. Blue and light-blue surfaces correspond to {111} and {100} faces, respectively. In the fcc network, the connectivity of 2D-nuclei on {111} and {100} faces were specified as three (denoted as THREE in green) and four (denoted as FOUR in yellow), respectively.

side pockets and cuboctahedral main pores. The cuboctahedral main pore is composed of square-windows and triangle-windows (Figure 2b). The main channels run along the ⟨100⟩ directions through the square-windows, while the neighboring tetrahedral side pockets can be accessed from the main pore through the triangle-windows along the ⟨111⟩ directions.

Here, we define a standard growth unit of $[Cu_3(btc)_2]_n$ to shape the main pore because it is composed of two significant channeling windows in the open-framework structure and involves all SBU orientations. This cuboctahedron standard unit is ideal and does not refer to the precise building unit formed in solution. However, by studying the relative growth rates of surface terraces, this would ultimately reveal the crystal morphology.

As the cuboctahedral growth unit associates with a maximum of twelve nearest neighboring sites in the network, those surface energies can be classified by their connectivities. Site types were named with numbers from ONE to TWELVE corresponding to the number of connectivity so that the energy levels are scaled in thermodynamics (visual-aid of site-type definition, see Figure S3, Supporting Information). By arranging the pore-network of $[Cu_3(btc)_2]_n$ in our coarse-grain model, a new simulation program was coded and run by site probabilities calculated from Gibbs free energy for each site type.

As shown in Figure 3, two site types, THREE and FOUR, became the dominant numbers of connectivity to produce 2D-nucleation on the {111} and {100} faces, respectively. Indeed, only by changing the relative energies between the THREE and FOUR sites did the simulated crystal morphology evolve from an octahedron to a cube by gradually exposing {100} faces (Figure 4). ΔE_i shows the energy difference between the site type i and the ideal equilibrium state. When $\Delta E_{THREE} > \Delta E_{FOUR}$, the simulated morphology became an octahedron, $\Delta E_{THREE} = \Delta E_{FOUR}$ a truncated octahedron, $\Delta E_{THREE} < \Delta E_{FOUR}$ a cuboctahedron, and $\Delta E_{THREE} \ll \Delta E_{FOUR}$ a cube. In the growth process, the site type FOUR is intrinsically more favored because the relative energy of FOUR is more stable than that of THREE (i.e., $\Delta E_{THREE} > \Delta E_{FOUR}$), leading to the fast growth along the ⟨100⟩ direction and the resulting octahedron morphology with the {111} surfaces. This is in agreement with the fact that most studies on the $[Cu_3(btc)_2]_n$ framework reported an octahedron crystal morphology.[17,27a,28,30] However, under altered experimental conditions, we might change the relative energy between THREE and FOUR and create an *unnatural* situation where $\Delta E_{THREE} < \Delta E_{FOUR}$, leading to the formation of cubic morphology. Considering our experimental conditions and the SEM observations (Figure 1), only the change in the modulator

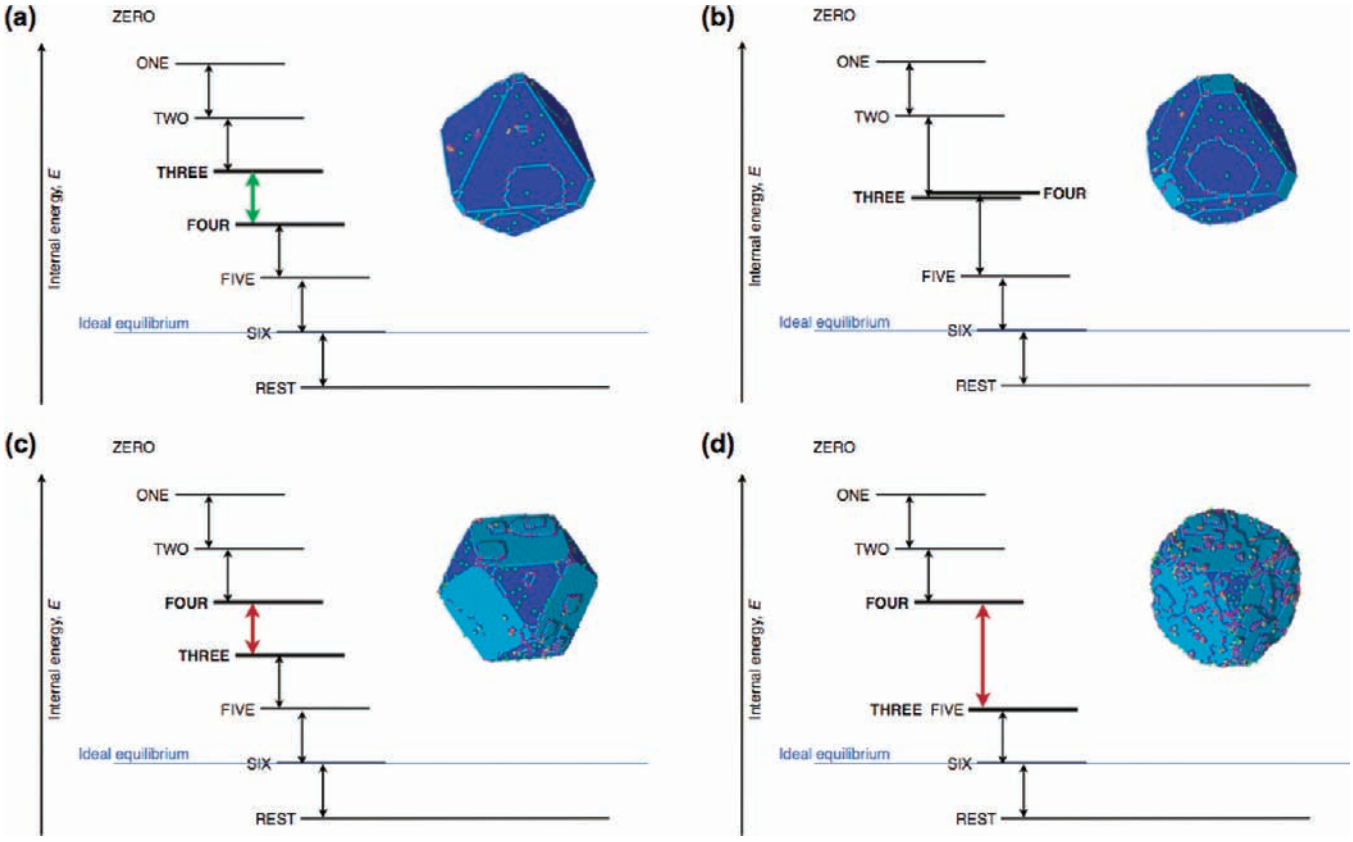

Figure 4. A series of crystal morphology controlled by relative energies at THREE and FOUR sites shown in the energy correlation diagrams. (a to d) Octahedron ($\Delta E_{THREE} > \Delta E_{FOUR}$) changes the shape appearing {100} as becoming $\Delta E_{THREE} \ll \Delta E_{FOUR}$. For the inset coarse-grain simulation images, red, pink, green, yellow, orange, purple, light-blue, and blue correspond to ZERO, ONE or TWO, THREE (i.e., 2D-nucleation on {111} facets), FOUR (i.e., 2D-nucleation on {100} facets), FIVE, SIX, SEVEN or EIGHT (i.e., {100} facets), and NINE to TWELVE (i.e., {111} facets), respectively.

concentration can account for the regulation of those relative energies.

Figure 5 shows a molecular-scale comparison between the THREE- and FOUR-attaching processes based on the cuboctahedron standard unit. This cuboctahedron unit is composed of 24 btc ligands where two carboxylates of each btc are involved in the construction of the cuboctahedron, while the remaining carboxylate is used to connect a neighboring site. In the case of THREE, six btc ligands, thus six carboxylates, contribute to the attachment on three neighboring sites. In contrast, FOUR requires the contribution from eight btc ligands to satisfy the connectivity. When adding monocarboxylic acid as a modulator of the growth process, the attachment of the growth unit will be perturbed because of the competition between the modulator and one of carboxylates in the btc ligand at the attachment event. One can consider that FOUR would be more strongly influenced by this perturbation than THREE because of the larger number of carboxylates involved in the attachment in FOUR. When the concentration of modulator is increased, the site type FOUR becomes less favored, which results in the destabilization of the relative energy of FOUR. This change in the relative energy would explain the transition of the crystal morphology.

Effect of Modulator on the Formation of Preorganized Paddlewheel Units and on the Resulting Morphology. As described above, we explained the effect of modulator on the crystal morphology transition by simply modeling the assembly based on the ideal cuboctahedron unit. In the experimental procedure, copper nitrate was first mixed with modulator prior to the addition of btc ligand, which presumably formed the preorganized paddlewheel unit as the SBU. Bearing in mind that crystal morphology is controlled at the early stage of crystal growth (Figure S2), it is important to investigate the influence of the structural features of metal precursors on the initial assembly process of metal ions and linkers.

In order to gain insight on the configuration of the metal precursor, we investigated the electronic absorption of stable copper−modulator mixtures. We prepared stable mixtures of copper nitrate and various amounts of lauric acid as the modulator. Figure 6 shows the electronic absorption spectra of the solutions of copper nitrate and lauric acid (the concentrations correspond to LA-0 to LA-125) in butanol. In all cases, a broad absorption band in the range of 600−900 nm was observed, which could be attributed to the d−d transition of the copper ions. The absorption maximum (λ_{max}) peaked at 790 nm when copper nitrate was solely dissolved (namely, LA-0) in butanol. When the concentration of modulator was increased to LA-25, and then to 50, 75, 100, and 125, the λ_{max} gradually blue-shifted to 775, 750, 740, 723, and 720 nm, respectively. Interestingly, the λ_{max} gradually approached that observed for copper acetate (λ_{max} = 702 nm) or copper laurate (λ_{max} = 695 nm) in butanol as shown in Figure 6 and Figure S4, Supporting Information. The lack of isosbestic point implies the presence of multiple intermediate species, the elucidation of which is beyond this study. However, the increase in concentration of modulator might

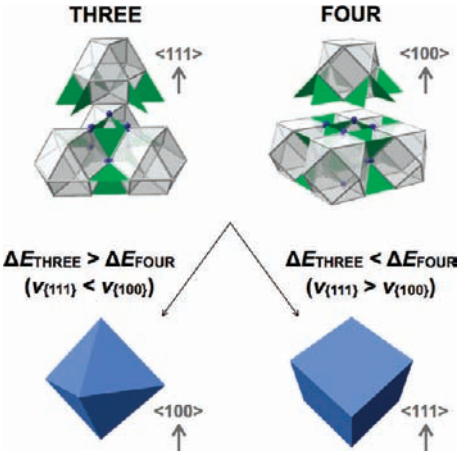

Figure 5. The THREE- and FOUR-attaching processes based on the cuboctahedron standard unit, showing six btc ligands (i.e., six carboxylate) contribute to the attachment on three neighboring sites, and eight on four neighboring sites, respectively. In the attaching processes, when the FOUR site is more stable to grow than the THREE site (i.e., $\Delta E_{THREE} > \Delta E_{FOUR}$), ⟨100⟩-growth will progress (i.e., $v_{\{111\}} < v_{\{100\}}$) and produce octahedral morphology while for the condition of $\Delta E_{THREE} < \Delta E_{FOUR}$, ⟨111⟩-growth will occur (i.e., $v_{\{111\}} > v_{\{100\}}$), resulting in cubic morphology.

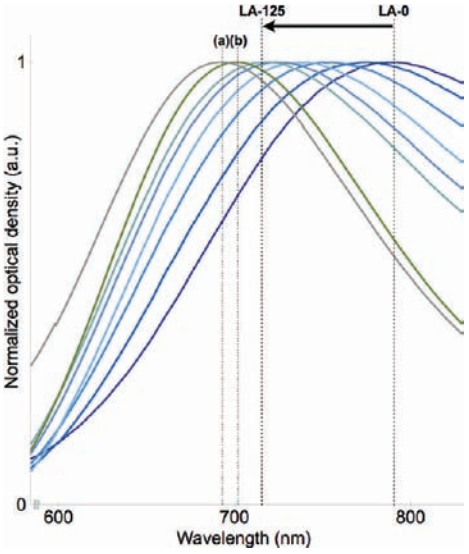

Figure 6. UV−vis spectrum showing the interaction of copper-metal sources and *n*-dodecanoic acid (modulator) in butanol. The λ_{max} shift from right (790 nm) to left (720 nm) corresponds to LA-*x*; $x = 0$, 25, 50, 75, 100, and 125, respectively, when the metal-source was copper nitrate. The λ_{max} (695 nm) shows copper laurate in butanol (a). The λ_{max} (702 nm) shows copper acetate with LA-0 (b).

induce a ligand-exchange reaction and gradually increase the population of the dinuclear copper paddlewheel cluster. Note that the shift of absorption can be correlated to the transformation of crystal morphology from octahedron to cuboctahedron and then cubic shapes. Namely, the absence of the preorganized paddlewheel structure (LA-0) in the metal precursor induces the octahedron morphology, while the high population of paddlewheel structure (LA-125) preferentially leads to the cubic crystal.

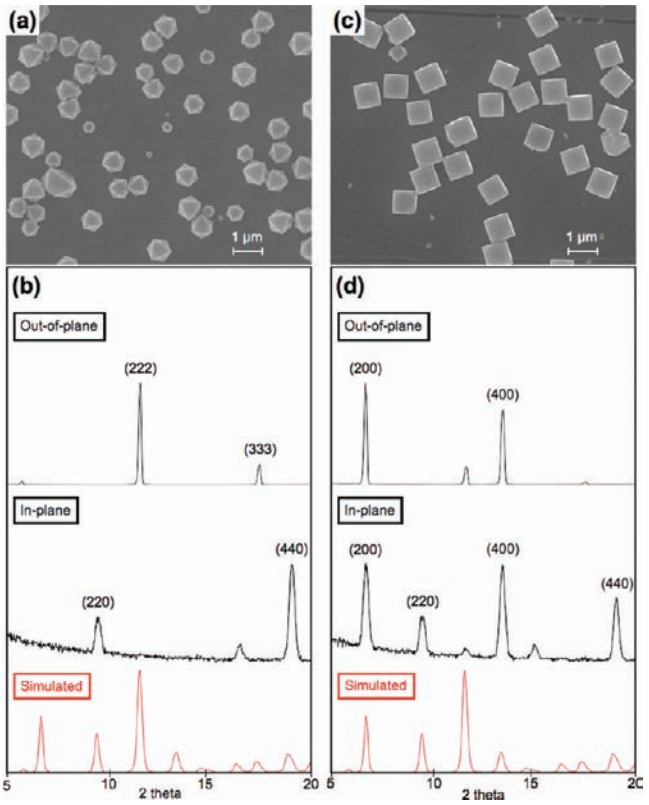

Figure 7. $[Cu_3(btc)_2]_n$ crystals grown on bare-gold-coated quartz substrates without function termini. (a) FESEM image of octahedron (LA-50) crystals immobilized on gold substrate and (b) corresponding X-ray diffraction patterns. (c) FESEM image of cube (LA-125) crystals immobilized on gold substrate and (d) corresponding X-ray diffraction patterns.

Note that the direction of coordination bonds between copper and carboxylate groups in the $[Cu_3(btc)_2]_n$ framework corresponds to the ⟨111⟩ direction. This fact implies that the ligand-exchange reaction of the preorganized paddlewheel precursor with btc would only accelerate the growth rate along the ⟨111⟩ direction. Hence, as the population of the preorganized paddlewheel structure is increased, the resulting crystal gradually exposes the {100} facets. This explanation is in agreement with our previous experiments; copper acetate only produces cubes of a well-defined morphology.[25]

Selective Crystal Orientation on Substrate Directed by Morphology Design. The patterning and immobilization of PCP crystals on a targeted substrate expands the feasibility of PCPs as functional materials. To date, the control of crystal orientation has been realized by chemical functionalization of the substrate (e.g., self-assembled monolayers, SAMs),[17a−d,27b,28,30d,30e] microcontact printing (e.g., lithographically controlled wetting, LCW),[17e] or dip-pen nanolithography.[30j] Here we demonstrate a straightforward method by taking advantage of the designability of crystal morphology by coordination modulation.

We developed a new method to produce either octahedral or cubic shape of $[Cu_3(btc)_2]_n$ crystals on a bare gold substrate under rather mild conditions (at 318 K without microwave-assisted heating). In order to produce the desired morphology, the precursor solutions were prepared by defined concentration of modulator (i.e., octahedral morphology at LA-50 and cubic morphology at LA-125, which corresponds to Figure 1c and 1f,

respectively). At such low temperature, the nucleation rate was significantly slowed. Therefore, ethanol as a counter solvent was added to the mother liquor to accelerate the nucleation. By simple immersion in these precursor solutions, $[Cu_3(btc)_2]_n$ crystals were formed on the gold substrate. Figure 7 illustrates the FESEM images and the corresponding X-ray diffraction patterns within 2θ of 5° and 20° of both samples. As we expected, only octahedron crystals were formed for LA-50 (Figure 7a) and only cubic crystals for LA-125 (Figure 7c). Interestingly, a well-balanced larger facet area of crystals preferably lies on the flat gold substrate. In Figure 7b, the out-of-plane orientation of octahedral crystals clarified two dominating peaks at $2\theta = 11.62°$ for {222} and 17.52° {333} and the corresponding in-plane orientation showed further evidential peaks at $2\theta = 9.51°$ {220} and 19.04° {440}. On the other hand, in Figure 7d, cubic crystals characterized at $2\theta = 6.68°$ {200} and 13.44 {400} for the out-of-plane orientation, and at $2\theta = 9.51°$ {220} and 19.09° {440} also for the in-plane orientation. Hence, the octahedron and cubic morphologies of the single crystals of $[Cu_3(btc)_2]_n$ induced the crystal orientation in ⟨111⟩ and ⟨100⟩ directions, respectively. This represents the first and straightforward example of selective orientations of PCPs on bare substrates governed by crystal morphology.

CONCLUSION

In summary, we focused on designing $[Cu_3(btc)_2]_n$ crystal morphology via coordination modulation and addressed a role of modulator in the crystal growth mechanism by coarse-grain modeling. First, we demonstrated the tendency of crystal morphologies of $[Cu_3(btc)_2]_n$ presenting an octahedron to a cube transition correlated to an increase in the concentration of modulator. Coarse-grain modeling revealed this morphology transformation with thermodynamic evidence calculated by a defined standard unit (cuboctahedral main pore) growing in favored directions. Considering the standard unit in a molecular scale during the coarse-grain attaching process allowed us to propose that the modulator acted as a growth-blocking agent, specifically on the site type FOUR, leading to the deceleration of the crystal growth in the ⟨100⟩ directions. Additionally, we suggested that the population of preorganized SBU controlled by the modulator concentration influenced the reaction kinetics to form a coordination bond between copper and btc oriented only in the ⟨111⟩ directions. Thus, the reaction with the btc from the paddlewheel copper complex was faster than that from copper nitrate and accelerated the growth in the ⟨111⟩ directions, consequently producing the {100} facets. This comprehensive study will enable us to design and produce well-defined desired PCP crystal morphology in a similar manner controlled by coordination modulation. Besides the importance of exposed crystal facets often discussed in catalytic activity, as another significance of the morphology design of PCPs, we presented a straightforward technique in crystal patterning with selective growth orientation on bare substrates. Further practical performance of PCPs depending on the crystal morphology is under current investigation for potential applications.

ASSOCIATED CONTENT

Supporting Information. Additional powder X-ray diffraction data, TEM data for the time-course UV−vis spectrum, site type definition of the coarse-grain model, and full author list for reference 11a. This material is available free of charge via the Internet at http://pubs.acs.org.

AUTHOR INFORMATION

Corresponding Author
shuhei.furukawa@kip.jst.go.jp; kitagawa@sbchem.kyoto-u.ac.jp

ACKNOWLEDGMENT

We acknowledge Prof. Osamu Terasaki (KAIST, Stockholm University), Dr. Yasuhiro Sakamoto (Osaka Prefecture University), Mr. Shunsuke Asahina (JEOL), Prof. Kensuke Akamatsu (Konan University), Prof. Hidemi Nawafune (Konan University), and Dr. Nobuhiro Morone (Kyoto University) for helpful advice on the SEM measurement.

REFERENCES

(1) (a) Mann, S. *Nature* **1988**, *332*, 119–124. (b) Yokoyama, E.; Kuroda, T. *Phys. Rev. A* **1990**, *41*, 2038–2049. (c) Libbrecht, K. G. *Rep. Prog. Phys.* **2005**, *68*, 855–895.

(2) (a) Wiley, B.; Sun, Y.; Chen, J.; Cang, H.; Li, Z.-Y.; Li, X.; Xia, Y. *MRS Bull.* **2005**, *30*, 356–361. (b) Liz-Marzán, L. M. *Langmuir* **2006**, *22*, 32–41.

(3) Ding, G. Q.; Shen, W. Z.; Zheng, M. J.; Xu, W. L.; He, Y. L.; Guo, Q. X. *J. Cryst. Growth* **2005**, *283*, 339–345.

(4) (a) Cosandey, F; Madey, T. E. *Surf. Rev. Lett.* **2001**, *8*, 73–93. (b) Limbach, L. K.; Wick, P.; Manser, P.; Grass, R. N.; Bruinink, A.; Stark, W. J. *Environ. Sci. Technol.* **2007**, *41*, 4158–4163.

(5) (a) Roeffaers, M. B. J.; Sels, B. F.; Uji-i, H.; Blanpain, B.; L'hoëst, P.; Jacobs, P. A.; De Schryver, F. C.; Hofkens, J.; De Vos, D. E. *Angew. Chem., Int. Ed.* **2007**, *46*, 1706–1709. (b) Roeffaers, M. B. J.; Ameloot, R.; Baruah, M.; Uji-i, H.; Bulut, M.; De Cremer, G.; Müller, U.; Jacobs, P. A.; Hofkens, J.; Sels, B. F.; De Vos, D. E. *J. Am. Chem. Soc.* **2008**, *130*, 5763–5772. (c) Schoonheydt, R. A. *Angew. Chem., Int. Ed.* **2008**, *47*, 9188–9191.

(6) (a) Yaghi, O. M.; O'Keeffe, M.; Ockwig, N. W.; Chae, H. K.; Eddaoudi, M.; Kim, J. *Nature* **2003**, *423*, 705–714. (b) Kitagawa, S.; Kitaura, R.; Noro, S. *Angew. Chem., Int. Ed.* **2004**, *43*, 2334–2375. (c) Ferey, G.; Mellot-Draznieks, C.; Serre, C.; Millange, F. *Acc. Chem. Res.* **2005**, *38*, 217–225. (d) Bradshaw, D.; Claridge, J. B.; Cussen, E. J.; Prior, T. J.; Rosseinsky, M. J. *Acc. Chem. Res.* **2005**, *38*, 273–282. (e) Wang, Z; Cohen, Z. M. *Chem. Soc. Rev.* **2009**, *38*, 1315–1329.

(7) (a) Kondo, M.; Yoshitomi, T.; Seki, K.; Matsuzaka, H.; Kitagawa, S. *Angew. Chem., Int. Ed.* **1997**, *36*, 1725–1727. (b) Rowsell, J. L. C.; Millward, A. R.; Park, K. S.; Yaghi, O. M. *J. Am. Chem. Soc.* **2004**, *126*, 5666–5667. (c) Millward, A. R.; Yaghi, O. M. *J. Am. Chem. Soc.* **2005**, *127*, 17998–17999. (d) Morris, R. E.; Wheatley, P. S. *Angew. Chem., Int. Ed.* **2008**, *47*, 4966–4981. (e) Dincá, M.; Long, J. R. *Angew. Chem., Int. Ed.* **2008**, *47*, 6766–6779.

(8) (a) Mueller, U.; Schubert, M.; Teich, F.; Puetter, H.; Schierle-Arndt, K.; Pastré, J. *J. Mater. Chem.* **2006**, *16*, 626–636. (b) Li, J.-R.; Kuppler, R. J.; Zhou, H.-C. *Chem. Soc. Rev.* **2009**, *38*, 1477–1504. (c) Couck, S.; Denayer, J. F. M.; Baron, G. V.; Remy, T.; Gascon, J.; Kapteijn, F. *J. Am. Chem. Soc.* **2009**, *131*, 6326–6327.

(9) (a) Fujita, M.; Know, Y. J.; Washizu, S.; Ogura, K. *J. Am. Chem. Soc.* **1994**, *116*, 1151–1152. (b) Hasegawa, S.; Horike, S.; Matsuda, R.; Furukawa, S.; Mochizuki, K.; Kinoshita, Y.; Kitagawa, S. *J. Am. Chem. Soc.* **2007**, *129*, 2607–2614. (c) Horike, S.; Dincá, M.; Tamaki, K.; Long, J. R. *J. Am. Chem. Soc.* **2008**, *130*, 5854–5855. (d) Lee, J.; Farha, O. K.; Roberts, J.; Scheidt, K. A.; Nguyen, S. T.; Hupp, J. T. *Chem. Soc. Rev.* **2009**, *38*, 1450–1459. (e) Ma, L.; Abney, C.; Lin, W. *Chem. Soc. Rev.* **2009**, *38*, 1248–1256. (f) Juan-Alcañiz, J.; Ramos-Fernandez, E. V.; Lafont, U.; Gascon, J.; Kapteijn, F. *J. Catal.* **2010**, *269*, 229–241.

(10) (a) Biemmi, E.; Darga, A.; Stock, N.; Bein, T. *Microporous Mesoporous Mater.* **2008**, *114*, 380–386.(b) Takashima, Y.; Martínz,

V. M.; Furukawa, S.; Kondo, M.; Shimomura, S.; Uehara, H.; Nakahama, M.; Sugimoto, K.; Kitagawa, S. *Nature Commun.* **2011**, *2*, 168.

(11) (a) Horcajada, P.; et al. *Nat. Mater.* **2009**, *9*, 172–178. (b) Taylor-Pashow, K. M. L.; Rocca, J. D.; Xie, Z.; Tran, S.; Lin, W. *J. Am. Chem. Soc.* **2009**, *131*, 14261–14263. (c) Mckinlay, A. C.; Morris, R. E.; Horcajada, P.; Férey, G.; Gref, R.; Couvreur, P.; Serre., C. *Angew. Chem., Int. Ed.* **2010**, *49*, 6260–6266.

(12) (a) Meek, S. T.; Greathouse, J. A.; Allendorf, M. D. *Adv. Mater.* **2010**, *23*, 249–267. (b) Shekhah, O.; Liu, J.; Fischer, R. A.; Wöll, C. *Chem. Soc. Rev.* **2011**, *40*, 1081–1106.

(13) Morris, R. E. *ChemPhysChem* **2009**, *10*, 327–329.

(14) Lee, C. Y.; Bae, Y.-S.; Jeong, N. C.; Farha, O. K.; Sarjeant, A. A.; Stern, C. L.; Nickias, P.; Snurr, R. Q.; Hupp, J. T.; Nguyen, S. T. *J. Am. Chem. Soc.* **2011**, *133*, 5228–5231.

(15) Ma, L.; Abney, C.; Lin, W. *Chem. Soc. Rev.* **2009**, *38*, 1248–1256.

(16) (a) Smolka, H. G.; Schwuger, M. J. *Colloid Polym. Sci.* **1978**, *256*, 270–277. (b) Dragčević, Z.; Subotić, B.; Bronić, J. *Tekstil* **1993**, *42*, 267–274.(c) Subotić, B.; Bronić, J. *Handbook of Zeolite Science and Technology*; Auerbach, S. M., Carrado, K. A., Dutta, P. K., Eds.; Marcel Dekker, Inc.: New York, 2003; Chapter 5, pp 129−203.

(17) (a) Hermes, S.; Schröder, F.; Chelmowski, R.; Wöll, C.; Fischer, R. A. *J. Am. Chem. Soc.* **2005**, *127*, 13744–13745. (b) Biemmi, E.; Scherb, C.; Bein, T. *J. Am. Chem. Soc.* **2007**, *129*, 8054–8055. (c) Gascon, J.; Aguado, S.; Kapteijn, F. *Microporous Mesoporous Mater.* **2008**, *113*, 132–138. (d) Zacher, D.; Shekhah, O.; Wöll, C.; Fischer, R. A. *Chem. Soc. Rev.* **2009**, *38*, 1418–1429. (e) Ameloot, R.; Gobechiya, E.; Uji-i, H.; Martens, J. A.; Hofkens, J.; Alaerts, L.; Sels, B. F.; De Vos, D. E. *Adv. Mater.* **2010**, *22*, 1–4.

(18) (a) Hartman, P.; Bennema, P. *J. Cryst. Growth* **1980**, *49*, 145–156. (b) Brent, R.; Cubillas, P.; Stevens, S. M.; Jelfs, K. E.; Umemura, A.; Gebbie, J. T.; Slater, B.; Terasaki, O.; Holden, M. A.; Anderson, M. W. *J. Am. Chem. Soc.* **2010**, *132*, 13858–13868.

(19) Eddaoudi, M.; Moler, D. B.; Li, H.; Chen, B.; Reineke, T. M.; O'Keeffe, M.; Yaghi, O. M. *Acc. Chem. Res.* **2001**, *34*, 319–330.

(20) Uemura, T.; Ono, Y.; Kitagawa, K.; S.; Kitagawa, S. *Macromolecules* **2008**, *41*, 87–94.

(21) Tsuruoka, T.; Furukawa, S.; Takashima, Y.; Yoshida, K.; Isoda, S.; Kitagawa, S. *Angew. Chem., Int. Ed.* **2009**, *48*, 4739–4743.

(22) Delgado-Friedrichs, O.; O'Keeffe, M.; Yaghi, O. M. *Acta Crystallogr., Sect. A: Found. Crystallogr.* **2006**, *A62*, 350–355.

(23) Chui, S. S.-Y.; Lo, S. M.-F.; Charmant, J. P. H.; Orpen, A. G.; Williams, I. D. *Science* **1999**, *283*, 1148–1150.

(24) Morris, R. E.; Bu, X. *Nat. Chem.* **2010**, *2*, 353–361.

(25) (a) Cuppen, H. M.; Meekes, H.; van Enckevort, W. J. P.; Bennema, P.; Vlieg, E. *Surf. Sci.* **2003**, *525*, 1–12. (b) Boerrigter, S. X. M.; Josten, G. P. H.; van de Streek, J.; Hollander, F. F. A.; Los, J.; Cuppen, H. M.; Bennema, P.; Meekes, H. *J. Phys. Chem. A* **2004**, *108*, 5894–5902.

(26) Diring, S.; Furukawa, S.; Takashima, Y.; Tsuruoka, T.; Kitagawa, S. *Chem. Mater.* **2010**, *22*, 4531–4538.

(27) (a) Biemmi, E.; Christian, S.; Stock, N.; Bein, T. *Microporous Mesoporous Mater.* **2009**, *117*, 111–117. (b) Shekhah, O.; Wang, H.; Zacher, D.; Fischer, R. A.; Wöll, C. *Angew. Chem., Int. Ed.* **2009**, *48*, 5038–5041.

(28) Zacher, D.; Liu, J.; Huber, K.; Fischer, R. A. *Chem. Commun.* **2009**, 1031–1033.

(29) Donnay, J. D. H.; Harker, D. *Am. Mineral.* **1937**, *22*, 446–467.

(30) (a) Chen, J.; Yu, T.; Chen, Z.; Xiao, H.; Zhou, G.; Weng, L.; Tu, B.; Zhao, D. *Chem. Lett.* **2003**, *32*, 590–591. (b) Alaerts, L.; Séguin, E.; Poelman, H.; Thibault-Starzyk, F.; Jacobs, P. A.; De Vos, D. E. *Chem.—Eur. J.* **2006**, *12*, 7353–7363. (c) Rowsell, J. L. C.; Yaghi, O. M. *J. Am. Chem. Soc.* **2006**, *128*, 1304–1315. (d) Shekhah, O.; Wang, H.; Kowarik, S.; Schreiber, F.; Paulus, M.; Tolan, M.; Sternemann, C.; Evers, F.; Zacher, D.; Fischer, R. A.; Wöll, C. *J. Am. Chem. Soc.* **2007**, *129*, 15118–15119. (e) Zacher, D.; Baunemann, A.; Hermes, S.; Fischer, R. A. *J. Mater. Chem.* **2007**, *17*, 2785–2792. (f) Shöâeè, M.; Agger, J. R.; Anderson, M. W.; Attfield, M. P. *CrystEngComm* **2008**, *10*, 646–648. (g) Guo, H.; Zhu, G.; Hewitt, I. J.; Qiu, S. *J. Am. Chem. Soc.* **2009**, *131*, 1646–1647. (h) Seo, Y.-K.; Hundal, G.; Jang, I. T.; Hwang, Y. K; Jun, C.-H.; Chang, J.-S. *Microporous Mesoporous Mater.* **2009**, *119*, 331–337. (i) Schlesinger, M.; Schulze, S.; Hietschold, M.; Mehring, M. *Microporous Mesoporous Mater.* **2010**, *132*, 121–127. (j) Carbonell, C.; Imaz, I.; Maspoch, D. *J. Am. Chem. Soc.* **2011**, *133*, 2144–2147.